Past fires and post-fire impacts reconstructed from a southwest Australian stalagmite

Liza K. McDonough[1,*], Pauline C. Treble[1], Andy Baker[2], Andrea Borsato[3], Silvia Frisia[3,2], Gurinder Nagra[4,2], Katie Coleborn[2], Michael K. Gagan[5,6], Sirine C. Fakra[7], David Paterson[8]

[1] ANSTO, Lucas Heights, NSW, 2234, Australia

[2] School of Biological, Earth and Environmental Sciences, University of New South Wales, Sydney, NSW, 2052, Australia

[3] School of Environmental and Life Sciences, University of Newcastle, NSW, 2308, Australia

[4] School of Earth, Energy and Environmental Sciences, Stanford University, CA, 94305, USA

[5] School of Earth, Atmospheric and Life Sciences, University of Wollongong, NSW, 2522, Australia

[6] School of Earth and Environmental Sciences, The University of Queensland, Brisbane, QLD, 4072

[7] Advanced Light Source, Lawrence Berkeley National Laboratory, Berkeley, CA, 94720, USA

[8] Australian Synchrotron ANSTO, Clayton, VIC, 3168, Australia

*Corresponding author: lizam@ansto.gov.au

Abstract:

Our current understanding of climate and its relationship to fires is generally confined to the recent past where instrumental records and satellite imagery are available. Speleothem records of past environmental change provide a unique opportunity to explore fire frequency and intensity in the past, and the antecedent climatic conditions leading to fire events. Here, we compare fire sensitive geochemical signals in a stalagmite from Yonderup Cave, a shallow cave in Western Australia, where well-documented wildfire events have occurred in recent decades. Principal component analysis of the stalagmite time-series revealed distinct peaks in a combination of phosphorus and metal (aluminium, zinc, copper and lead) concentrations, interpreted to have come from ash, in response to known fire events. This method is extended to identify fires during the growth interval of the speleothem (1760 CE–2005 CE). We identify lower and less variable peak phosphorus concentrations in the pre-European period that are consistent with low-intensity cultural burning by Indigenous Australians. We also identify an intense wildfire event occurring around 1897 ± 5 CE. The combination of climate and fire sensitive proxies in the speleothem indicates that this wildfire was preceded by a multi-decadal dry period. We interpret that post-fire changes in surface-cave hydrology resulted from heat-induced deformation of the shallow karst bedrock brought about by the intensity of this fire. These findings have implications for the interpretation of speleothem records from shallow caves in fire-prone climates and show the potential for speleothems to provide records of fire intensity and recurrence intervals. Further development of these records could lead to a better understanding of the climate-fire relationship and the effects of land-management practices on wildfire frequency and intensity.

1. Introduction

Wildfires are becoming progressively more extreme due to climate and land use changes (Moreira et al., 2020). Catastrophic wildfires such as those observed in Australia between

October 2019 and February 2020, during which nearly 17 million hectares of land were burned are occurring with increasing frequency. In the Northern hemisphere, in 2020 more than 4% of the total 100 million acres of the state of California land were burned. Karst systems, where caves host speleothems (e.g., stalagmites, stalactites and flowstones), can provide long-term records of changes in climate and the environment (e.g. Bar-Matthews et al., 1997; Cheng et al., 2016; Dorale et al.,1998; Hellstrom et al., 1998; Hopley et al., 2004; Wang et al., 2008). The impact of wildfires on dripwater and soil in karst systems is becoming increasingly well understood (Nagra et al., 2016; Bian et al., 2019; Coleborn et al., 2016; Treble et al., 2016), and suggests that speleothems may have the potential to provide records of fire frequency and intensity. Utilising stalagmites as proxies for paleo-fire could provide much-needed baseline information for the pre-satellite period, including the timing of human arrival in a region, and the relationship between humans, climate and fire. This information would provide a better understanding of ecosystem resilience and inform land-management policy.

Fires have the potential to alter soil properties and soluble element concentrations, which in turn affects soil leachate and dripwater chemistry. Changes in soil and ash leachate chemistry are impacted by the type of vegetation burnt and the burn intensity (Harper et al., 2019; Heydari et al., 2017; Hogue and Inglett, 2012; Plumlee et al., 2007; Quigley et al., 2019). Low to moderate intensity fires, such as prescribed burns, have been shown to result in increasing soil nutrients, whilst high intensity wildfires can potentially result in a reduction in nutrients due to volatilisation (Bodí et al., 2014; Certini, 2005). Post-fire increases in soil nitrogen (N) and phosphorus (P) and sulphur (S) have been noted in a number of studies (Butler et al., 2018; Grove et al., 1986; Schaller et al., 2015; Spencer et al., 2003), as well as increases in organic matter (OM) and sediment flushed into waterways after fires (Mast and Clow, 2008; Petticrew et al., 2006; Revchuk and Suffet, 2014; Ryan et al., 2011). These changes at the surface translate into changes in dripwater chemistry, and can ultimately impact on speleothem composition. For example, short-term increases in dripwater elements

such as S have previously been observed post-fire due to release of S from burnt vegetation (Bian et al., 2019) and evaporative concentration (Nagra et al., 2016). Decreases in S post-fire have also been observed due to nutrient limitation during forest regrowth (Treble et al., 2016), as well as temporary enrichment of dripwater $\delta^{18}O$ resulting from the evaporative loss of stored karst water (Nagra et al., 2016).

Temperatures at the base of a large wildfire can exceed 1000 °C (Wotton et al., 2012). Temperatures above 500 °C can affect the structural properties of limestone (Meng et al., 2020; Wu and Wang, 2012) leading to the creation and/or widening of microfractures in the epikarst (the upper weathered region of bedrock beneath the soil) due to extreme heating and cooling. The potential increase in transmissivity between the surface and cave could reduce the concentration of bedrock-derived elements dissolved in dripwaters. Conversion of limestone into lime (CaO) at high temperatures (> 900 °C, Moropoulou et al., 2001) may also increase meso- and macro-porosity while decreasing micro-porosity of the calcined rock (Valverde et al., 2015; Wang et al., 2019). When lime is subsequently mixed with water (e.g. rainwater), the most reactive CaO particles dissolve first, producing a high level of supersaturation (Kemperl and Macek, 2009) and increasing dripwater pH and supersaturation with respect to calcite (Hartland et al., 2010). This favours calcium carbonate precipitation in the cave, thus speleothem growth rate, which may be further enhanced by an increase in infiltration and drip rate due to loss of vegetation (Genty and Quinif, 1996; Nagra et al., 2016; Weber et al., 2018). The creation of a hydrophobic soil layer may further increase preferential flows through the soil as excess water is unable to be retained in the soil (Bian et al., 2019; DeBano, 2000; Stoof et al., 2014, Savage, 1974).

Speleothems from shallow caves are potentially ideal for studying the impacts of fires as confounding factors such as long infiltration pathways, lag times and the mixing of stored water with post-fire infiltration are minimised (Bian et al., 2019). In this study, we identify the geochemical ‘fingerprint’ of a fire event by comparing the speleothem geochemical record

with the known fire history, and extend this information to construct a 245 year record of paleo-fire events.

Yonderup Cave in Yanchep National Park (YNP), south-west Western Australia (WA), is a shallow cave (6 m depth) in a region affected by wildfires. An environmentally significant trace element record was produced from a stalagmite (YD-S2) in Yonderup Cave spanning the 20th century (Nagra et al., 2017). A hydrochemical response in dripwater from the cave was detected following a fire event that occurred whilst the cave was monitored (Nagra et al., 2016), suggesting that this cave is ideal for examining changes in speleothem geochemical composition caused by wildfires. Here, we present a longer and improved record from YD-S2, which includes new parameters bromine (Br), sulphur (S) and colloidal material. This record is developed through the use of 1D (i.e. line plot) time-series (Nagra e.al., 2017), and lamina counts obtained from 2D elemental and physical maps. We here include an assessment of speleothem $\delta^{18}O$, $\delta^{13}C$, colloidal material including OM, and trace elements S and Br, and extend the chronology back to 1760 CE. We hypothesize that high intensity fire events result in pulses of ash-derived elements and an increase in infiltration from the surface to the cave due to porosity changes and increased preferential flows resulting from the formation of a hydrophobic soil layer. The increased drip rate combined with supersaturation of the dripwater with respect to calcite caused by the calcination of the limestone is likely to lead to increased speleothem growth rate after intense fires.

2. Environmental Setting

2.1. Geology

Stalagmite YD-S2 was fed by an actively dripping stalactite before its removal and commencement of dripwater monitoring in July 2005 (Nagra et al., 2016, Site 1a). Yonderup Cave is located approximately 47 kilometres north-northwest of Perth in YNP, Western Australia (Figure 1). It is developed in the Tamala Limestone lithostratigraphic unit, an extensive Pleistocene aeolianite (Playford, et al., 1976; Playford, et al., 2013), outcropping

along the coast of southwest Western Australia. The lithology of the Tamala Limestone consists predominantly of aeolianite, with subordinate interbedded paleosols, calcrete and microbialite (Lipar and Webb, 2014). The aeolianite is comprised predominantly of carbonate and quartz, as well as smaller amounts of detrital microcline and orthoclase feldspar (Lipar and Webb, 2014). The carbonate bioclasts within the aeolianite consist of high magnesium (Mg) calcite and aragonite, both of which commonly transform into low-Mg calcite, which is the predominant phase in the diagenised aeolianite. Calcarenites of the Tamala Limestone show a progressive reduction in aragonite and high-Mg calcite content with increasing age, and a corresponding increase in low-Mg calcite content. Critically, the Tamala Limestone was subjected to meteoric diagenesis with eogenetic karst development, which resulted in rapid transmissivity owing to a dual-pore system.

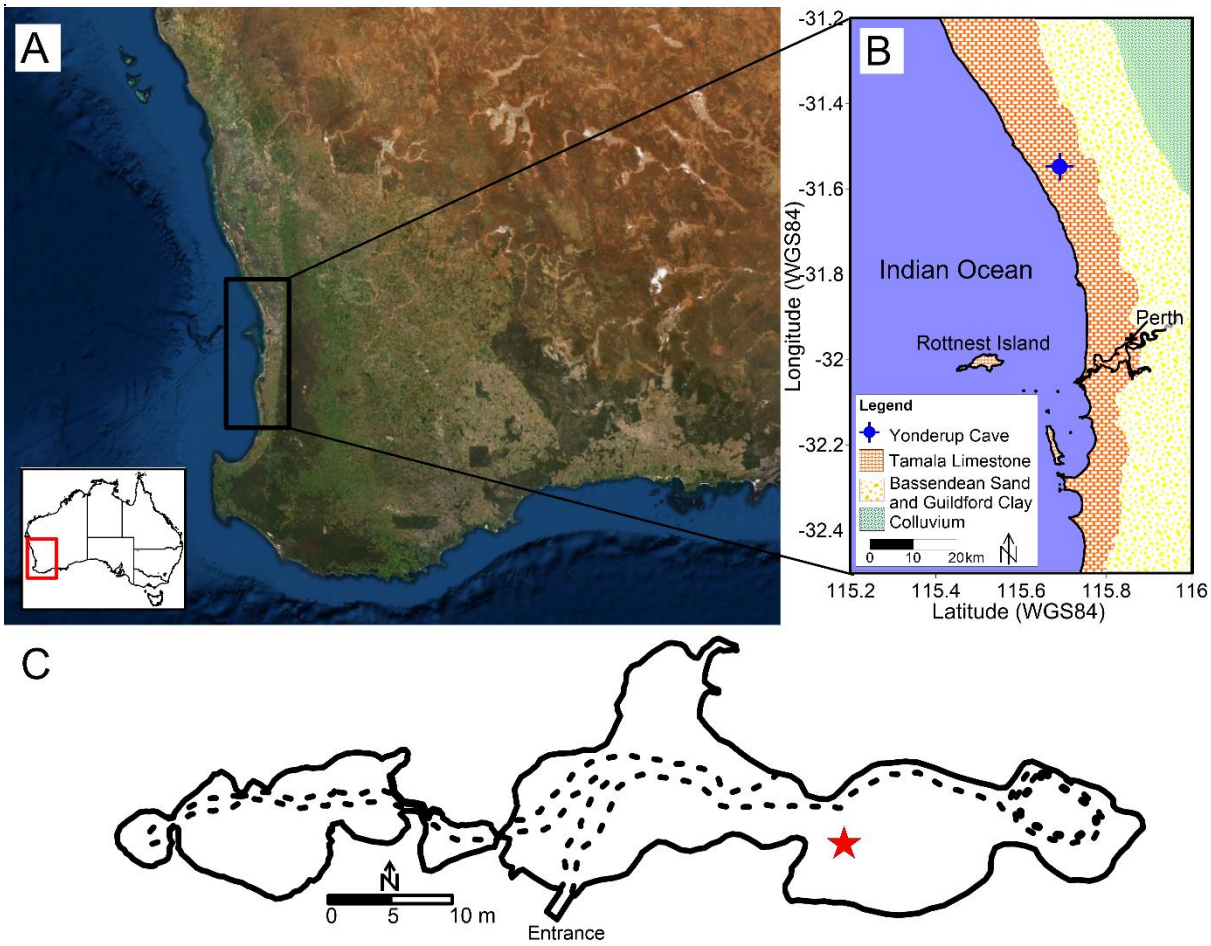

Figure 1. A) Map of study region with B) inset showing the location of Yonderup Cave and extent of the Tamala Limestone (adapted from Smith et al., 2012). C) Plan view of Yonderup Cave showing tourist pathways as dashed lines (State Records Office of Western Australia, 2015) and location of stalagmite YD-S2 (red star).

2.2. Climate characteristics and fire-history

The climate at Yanchep is classified as Mediterranean with hot, dry summers and cool, wet winters. The Australian Bureau of Meteorology manages a weather station (number 009053) located approximately 34.5 km south-east of the study site, which has recorded long-term temperature (1940–2020 CE) and precipitation (1937–2020 CE) data. The long-term average rainfall rate is 628 mm year^{-1} ± 168 (1 σ), with most (60%) of the rain falling during winter and a small proportion (5%) falling during summer. The long-term average maximum and minimum temperatures are 25.3 ± 1.4 °C (1 σ) and 12.4 ± 1.0 °C (1 σ). A drying trend is reported in the period after 1970 CE with a further decrease in rainfall after 1990 CE (Hope et al., 2010).

The Yanchep region is prone to the occurrence of wildfires in summer due to low rainfall, frequent lightning storms and abrupt wind changes caused by pre-frontal troughs (McCaw et al., 2003). A number of fire events in the recent past within the bounds of the YD-S2 record are known to have occurred at YNP. These include three prescribed burns that burned above or in very close proximity (<10 m) to Yonderup Cave in 1966 CE, 1996 CE and 2001 CE (Figure S1; Nagra et al., 2017). A wildfire in 2005 CE also burnt directly over the cave approximately 6 months prior to the collection of YD-S2 (Figure S1). Two other wildfires are also reported to have occurred in the broader YNP region in 1977 CE and 1983 CE and burnt 500 ha, 800 ha (Department of Environment and Conservation, 2010). Satellite imagery reveals in the next that the 1983 CE fire burnt to the north-west of the cave (Figure S1). Imagery for the 1977 CE event is unavailable, and it is unclear whether this fire burned directly over the cave.

2.3. Indigenous and European history

Pre-European vegetation near the cave area is classified as low forest and woodland (< 10m tall) consisting of wattle, banksia, peppermint, cypress pine, casuarina and York gum (Beard, et al., 2013). Areas of medium forest woodland (10 – 30m tall), scrub heath and thicket were present to the west of the caves towards the coast (Beard, et al., 2013). Current vegetation consists of tuart (*Eucalyptus gomphocephalla*) forest, banksia heath and wetland vegetation.

Traditionally, Yanchep was a meeting place for the Noongar people prior to European settlement. It was chosen for its proximity to the coast, lake, forest and wetland areas, which contained abundant resources. The area has mythological, ritual and ceremonial significance for Australia's First People (Department of Conservation and Land Management, 1989). The first documented account of Europeans visiting Yanchep was in 1834 CE (Department of Conservation and Land Management, 1989). In 1835 CE a stock route was established and used by drovers however the Yanchep area was not settled by Europeans until 1901 CE (Department of Conservation and Land Management, 1989). Most of the caves in YNP were discovered and explored shortly thereafter in 1904 CE (Department of Conservation and Land Management, 1989). In 1932 CE Yonderup Cave was officially opened to the public as a tourist attraction.

3. Methods

Stalagmite YD-S2 was analysed using a number of different methods including synchrotron based x-ray fluorescence (XRF) elemental mapping, excimer laser ablation inductively-coupled plasma mass spectrometry (LA-ICP-MS), thin section scans for colloidal particulates (including OM) and stable isotope ($\delta^{13}C$, $\delta^{18}O$) analyses. YD-S2 was sectioned in half along the central growth axis using a 2 mm wide diamond blade. One half was sub-sampled for U/Th analyses, which are presented in Nagra et al. (2017). The remaining half was sectioned along the growth axis to produce adjacent slabs for stable isotope ratios and for elemental analysis. Synchrotron XRF and LA-ICP-MS were conducted on the same polished

slab and the thin section was cut from the back of this slab. The presence of laminae visible to the unaided eye permitted verification that sampling depth was comparable across the sub-sampled pieces for different analytical techniques. Details for the methods are provided below.

3.1. Synchrotron micro-focused X-Ray fluorescence

We undertook synchrotron XRF elemental mapping of calcium (Ca), bromine (Br), strontium (Sr) and zinc (Zn) at The Australian Synchrotron, Australian Nuclear Science and Technology Organisation (ANSTO) in Melbourne at a 2µm resolution using a monochromatic incident energy of 18.5 keV, the beam was focused to a spot size of 1.5 µm on the sample, and a dwell per pixel from 1 to 4 milliseconds (ms) was used. XRF elemental maps were collected using a Maia 384 (Sync) – HYMOD detector with data reduced at the Australian Synchrotron using CSIRO Dynamic Analysis method and GeoPIXE software. Counts were then analysed to obtain true-elemental images in absolute values as parts per million (ppm) (Ryan et al., 2005; Ryan et al., 1995). ImageJ (https://imagej.nih.gov/ij/) was then used to extract time-series of absolute concentrations at 2 µm intervals perpendicular to the growth laminae using a 20-pixel line width. A 13-point Savitsky-Golay filter was applied to the Br map to reduce noise in the dataset that could obscure the long-term trends, whilst also preserving the peaks and troughs.

XRF elemental maps of light elements (S, Mg and P) were recorded at beamline 10.3.2 (Marcus, et al., 2004) of the Advanced Light Source (Lawrence Berkeley National Laboratory, Berkeley, California, USA) using a 10 x 10 µm pixel size, a 200 millisecond dwell time/pixel, an incident photon energy of 3988 eV (50 eV below the Ca K-edge) and a beam spot size of 7 x 7 µm. The maps were recorded with an Amptek FAST XR-100SDD single element detector. Maps were then deadtime corrected and extracted with custom LabVIEW software available at the beamline A line plot of the scan was obtained from ImageJ and relative concentrations at 10 µm intervals were exported to excel. Absolute concentrations

could not be determined for P, Mg and S owing to a lack of matrix-matched standards at the time of these measurements.

3.2. LA-ICP-MS

Aluminium (Al), barium (Ba), uranium (U), zinc (Zn), copper (Cu), lead (Pb), phosphorus (P), magnesium (Mg) and strontium (Sr) elemental data were analysed using excimer laser ablation inductively-coupled plasma mass spectrometry (LA-ICP-MS) at The Australian National University (ANU) according to the methodology reported in Nagra et al. (2017). A motorised stage was used to acquire data in continuous scanning mode at 0.5 mm min^{-1} with laser firing at 15 Hz and masked to 5 x 35 µm slit with the wider axis orientated perpendicular to the growth axis. The LA-ICP-MS data show more defined peaks and troughs compared to the synchrotron line scans obtained from ImageJ for P, Mg and Sr. Therefore, the LA-ICP-MS data was selected for use in the principal component analysis (PCA) for these elements over the line plots obtained from the synchrotron scans. A comparison of the synchrotron and LA-ICP-MS results is shown in Figure S2.

3.3. Speleothem fabric and colloidal organic matter

Speleothem fabrics were observed via optical microscopy on 30 µm thick thin sections using a Zeiss Axioplan and Leica MS16 stereomicroscope at the Speleothem Microscopy Laboratory at the University of Newcastle, Australia. Fabrics were described and coded following a conceptual framework of fabric development reflecting changes in the cave environmental parameters (Frisia, 2015). The entire thin sections were imaged using a flatbed scanner Epson Perfection V550 with a resolution of 2540 dpi, which is sensitive to fabric changes such as porosity and impurities as determined by optical microscopy. Relative colloidal concentrations were then extracted from the thin section scan as greyscale variations using ImageJ, whereby darker brown bands (low greyscale) represent higher colloidal material. These values were inverted by subtracting each value from 250 to display high values as relatively high relative colloidal concentrations. The extraction of the

greyscale values was performed in ImageJ along the growth axis (parallel to the lamination). Where cracks in the thin section lamina were present, these occurred diagonally, therefore the corresponding values were extracted along parallel lines on the right or left side of the master line in order to avoid the damaged area.

3.4. Stable isotope ratios

Speleothem $\delta^{18}O$ and $\delta^{13}C$ were analysed at the Research School of Earth Sciences, ANU. Powders were continuously milled along the edge of the growth axis using a 2 mm diameter tungsten carbide end-mill bit, effectively shaving samples at 0.1 mm increments, following the method of Gagan et al. (1994). A 'clear cut' was made at each increment by milling an additional 1 mm into the sample to account for the curvature of the bit before cutting the next sample. 180–220 µg samples were weighed and analysed using a Finnigan MAT-251 dual-inlet stable-isotope ratio mass spectrometer coupled to a Kiel I micro-carbonate preparation device. Analyses were calibrated using the National Bureau of Standards NBS-19 standard ($\delta^{18}O_{VPDB}$ = −2.20‰ and $\delta^{13}C_{VPDB}$ = +1.95‰). A further linear correction for $\delta^{18}O$ was made using the NBS-18 standard ($\delta^{18}O_{VPDB}$ = −23.0‰). The original delta values for NBS-19 and NBS-18 are used to maintain consistency of results through time in the RSES Stable Isotope Laboratory. Long-term measurement precision for NBS-19 at the time of measurements was ±0.07‰ (2 σ) for $\delta^{18}O$ and ±0.04‰ (2 σ) for $\delta^{13}C$.

3.5. Chronology

A chronology for YD-S2 (0–12.15 mm distance from top; DFT) was already obtained by Nagra et al. (2017) by using one dimensional LA-ICP-MS line scans. In the two-dimensional dataset presented here (covering 0–18.87 mm DFT), the clearest laminae information was visible in the thin section and from the synchrotron map for Sr concentrations (Figure S3). Accordingly, development of the chronology was primarily based on visible laminae on the thin section in the region of 0 mm–18.87 mm DFT. These were verified against the Sr XRF

maps, and for a few laminae (< 5% of the total laminae across the 18.87 mm area of interest), Sr bands were used as the primary counting method due to low amounts of colloidal material.

3.6. Statistical analysis

Shapiro-Wilk's tests for normality were performed in RStudio (v.1.1.456) on individual variables. All variables returned a p value <0.05 suggesting that the distributions are significantly different from normal. Non-parametric Spearman's correlations were therefore used to assess correlations between variables in the results section. The mean peaks in P pre- and post-1900 CE were compared using a two sample t-Test assuming unequal variances.

Change-points in the mean and variance of the data were examined with RStudio (v.1.1.456) changepoint package using a binary segmentation method (Scott and Knott, 1974) and pruned exact linear time (PELT) method (Killick et al., 2012). The PELT method reportedly has increased accuracy relative to other change-point identification methods (Killick et al., 2012), however it was only suitable for assessing Mg variability. For the other time-series it resulted in an identification of almost all values as change-points. In these instances, the binary segmentation method was used.

In order to assess the longer-term changes that we hypothesise could have occurred from changes in hydrology following a fire, PCA was performed on the YD-S2 time-series data. Data from 1897 CE were excluded due to the observation of unusually large short-term peaks in parameters P, Mg, $\delta^{13}C$ and $\delta^{18}O$. For P, Mg, Sr, Ba, U, $\delta^{13}C$ and $\delta^{18}O$ data, we used the time-series utilised in Nagra et al. (2017). The colloid/OM and XRF Br and S time-series were obtained from thin section and XRF maps respectively after processing in ImageJ. Data were linearly interpolated to the resolution of the stable isotope ratio data (100 µm intervals) in OriginPro v.9.7.5.184. PCA was then performed in Python using *sklearn.decomposition.PCA*, with the loadings of each parameter on the leading principal

components, and changes in the principal component values over time assessed. Metals (Cu, Pb, Zn, and Al) were removed from the PCA when assessing the longer-term variability in hydrology, as they reduced the total percent variance explained by the first two components from 65.9% to 51.8%.

Peaks in soil-derived parameters P and OM on PC3 were further investigated to determine whether PC3 can shed light on potential fire events which should result in a pulse of ash-derived elements deposited on the soil. In order to achieve this, all variables were interpolated to high resolution LA-ICP-MS data (0.63 µm intervals), with U, Br and $\delta^{13}C$ data smoothed using a rolling median (window size = 50). The PCA was then re-run to include the 1897 CE data and metals Cu, Pb, Zn and Al.

Biplots were generated in RStudio (v.1.1.456) using the PCA() and fviz_pca() functions of the FactoMineR (Lê et al., 2008) and factoextra (Kassambara and Mundt, 2020) packages. Groups are based on k-means using the loadings of each variable on the PCA components, whereby variables are assigned to a cluster based on Euclidean distances between the variable and the closest cluster centroid. Variables within the same cluster have high intra-class similarity of loadings on the PCA components.

4. Results

4.1. Chronology building

The upper 18.87 mm of stalagmite YD-S2 contains visible, flat and parallel laminae over a width of at least 20 mm. Darker bands in the thin section indicate relatively higher colloids. These likely consist of OM as shallow cave depths result in negligible OM filtering effects (cf. Frisia and Borsato, 2010) (Figure S4). Nagra et al. (2017) identified that dripwaters at the YD-S2 site experience seasonal fluctuations in Sr concentrations as a result of prior calcite precipitation, however we identify a negative seasonal relationship between Mg and Sr in speleothem YD-S2 suggesting an additional process affecting Sr during incorporation into the speleothem (see Section 5.1). Alternating dark and light bands coincide with low and

high Sr concentrations, respectively, demonstrating that a higher proportion of colloids/OM incorporated into the speleothem is associated with low incorporation of Sr. This points to low supersaturation of the drip with respect to calcite during the wet season at this site. The appearance of seasonal colloidal particulates in YD-S2 is consistent with highly seasonal recharge and a short flow path length implying relatively fast transmission from the soil zone.

A total of 246 ± 12 annual layers were counted in the upper 18.87 mm of YD-S2 using the combined images of colloids/OM in the thin section and the Sr XRF maps. This results in an age span from 1760 ± 13 CE to the known collection date of July 14th 2005 CE at 0 mm DFT (Figure 2). Complex stratigraphy below 18.87 mm prevents the interpretation of the earlier YD-S2 paleo-environmental record.

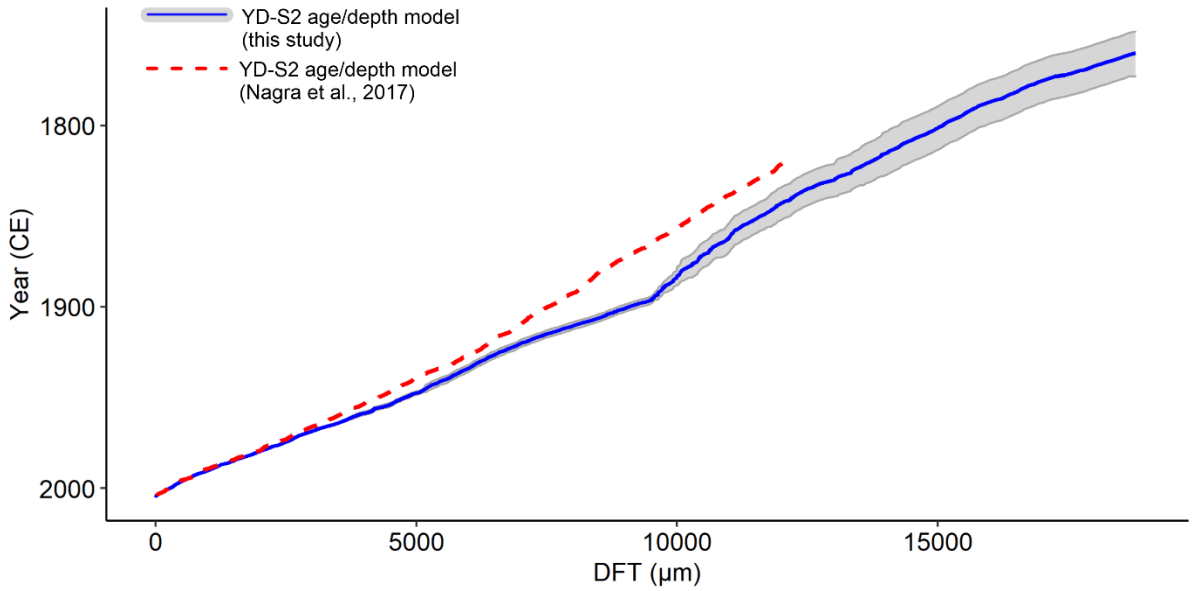

Figure 2: Chronology of YD-S2 based on lamina counts. Lamina age (Year CE) is shown on y-axis and distance from the top (DFT µm) of the speleothem shown on the x-axis. Grey shading shows the envelope of uncertainty for the lamina counts. Red dashed line represents the chronology as reported in Nagra et al. (2017).

Figure 2 shows the previous chronology developed by Nagra et al. (2017) for YD-S2 developed on LA-ICP MS line scan (1D) data between 0 – 12.15 mm DFT. Nagra et al.

(2017) use an automated peak-finding method based on peaks in multiple transects of Ba, Sr and U to determine a date of 1818 CE at the maximum DFT (12.15 mm). In contrast, the lamina counting method employed here identifies an age of 1841 CE at the same depth. Both chronologies are within the published U/Th age uncertainty at 8.10 mm DFT and 12.15 mm DFT where initial $^{230}Th/^{232}Th$ activity ratios of 1.5 and 1.33 are used (Nagra et al., 2017), however it does suggest that over-counting may occur when fitting peaks based exclusively on 1D time-series data (LA-ICP-MS tracks). The Nagra et al. (2017) chronology assumed a missing peak resulting from poorly defined annual cycles if no peak was identified within two times the average annual growth rate and there is variation of > 30% of the average peak height, which could result in additional peaks being counted. The identification of laminae from 2D maps used here is expected to reduce these types of user error due to availability of the whole map as opposed to individual transects.

Laminae counting and error estimate in this study was made by determining the position of the colloidal laminae and Sr peaks on thin section images and synchrotron Sr maps at five confidence levels (> 95%, 75–95%, 50–75%, 25–50%, 5–25%, and < 5% confidence) using ImageJ software package (Faraji, et al., 2021). The calculated error is up to 13 years for 1760 CE to 1887 CE, and up to 4 years for 1888 CE to 2005 CE.

4.2 Extension rate

The average annual vertical axis extension rate for YD-S2 is 77 ± 30 µm yr^{-1} (1σ). Change-point analysis shows a high mean extension rate occurred in 1760–1775 CE (116 ± 26 µm yr^{-1}, 1σ). The rate decreases between 1775–1854 CE (72 ± 23 µm yr^{-1}, 1σ) (Figure S5, Table S1) and then drops to the lowest rate observed in the data between 1854 and 1896 CE (44 ± 23 µm yr^{-1}, 1σ). A pronounced long-term shift to higher extension rates occurs after 1896 CE (Figure S5, Table S1) and declines after 1995 CE.

4.3 $\delta^{18}O$, $\delta^{13}C$, minor and trace elements

There is a strong correlation between $\delta^{18}O$ and $\delta^{13}C$ values for the entire dataset ($r_s = 0.85$, $p < 2.2 \times 10^{-16}$), which is weaker during the period 1900–1940 CE ($r_s = 0.52$, $r_s < 2.2 \times 10^{-16}$). A positive correlation between $\delta^{18}O$ and Mg ($r_s = 0.56$, $p < 2.2 \times 10^{-16}$), $\delta^{13}C$ (rs = 0.72, < 2.2 x 10^{-16}) and Br ($r_s = 0.54$) is observed. All of these proxies show higher mean values from the late 1820s, generally followed by a shift to lower overall mean values from the late 1890's CE ($\delta^{18}O$, $\delta^{18}O$ and Mg) and 1911 CE (Br) as supported by change point analyses (Table S1). Additionally, Mg and stable isotopes ($\delta^{18}O$ and $\delta^{13}C$) display a short-lived maxima at 1897 CE and 1898 CE respectively, during or immediately after the occurrence of a large peak in P concentration. These parameters abruptly shift to the lowest mean concentrations thereafter.

Figure 3 indicates that S and Ba mean concentrations increase from approximately 1870 CE to the mid-1880's CE. Concentrations of both elements rapidly drop in the mid 1880's CE, approximately 11 years prior to the peak in P in 1897 CE (Figure S5, Table S1). Change-points indicate that Ba, Sr and S mean concentrations begin to rise after the mid to late-1980's CE. Change-points in the mean are not detected in the U data, likely due to high variability in the dataset. Significant correlations ($p < 2.2 \times 10^{-16}$) are, however, observed between Ba and U ($r_s = 0.61$), Ba and S ($r_s = 0.74$), S and U ($r_s = 0.56$), Sr and S ($r_s = 0.66$) and Sr and Ba ($r_s = 0.62$) (Table S3).

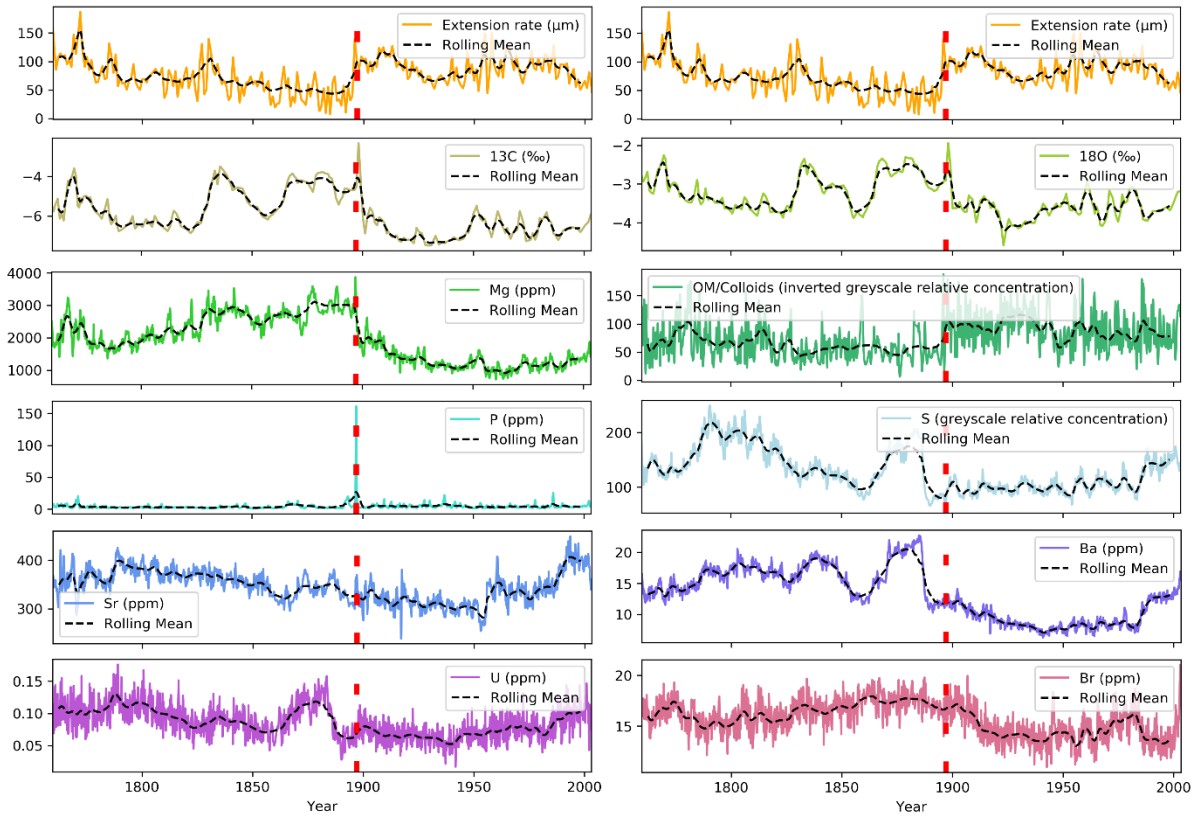

Figure 3: Time-series of extension rate (top panel) and geochemical variables included in the PCA. The 1897 CE event is marked by a red dashed line. The black dashed lines represent an approximately 5-year (window size = 100) rolling mean concentration.

4.4 1897 CE event

The sudden shift in the extension rate after 1896 CE closely coincides with a change in mean values for other climate and environmental proxies: i. a maximum in $\delta^{18}O$ and $\delta^{13}C$ in early 1898 CE (-1.9‰ and -2.3‰ respectively); ii. an abrupt peak in Mg concentration (4527 ppm), followed by a 70% decrease in mean Mg concentrations by 1900 CE that then remain low (Figure 3, Figure S5, Table S1); iii. an abrupt increase in the mean relative abundance of colloids/OM in 1897 CE (Table S1), and iv. a clear maximum in P in 1897 CE (Figure 3), with the value reaching 161.2 ppm (more than 5 times the median concentration, Table S2).

The fabric immediately prior to the 1897 CE event (< 1 year, 9.35 – 9.45 mm DFT) is defined by a micro-hiatus or very slow deposition of compact calcite crystals (see thin section in

Figure 4 and Figure S3). There appears to be continuity in crystal growth before and after this “micro-hiatus” and erosion of crystal tips is not evident, which suggests that the feeding drip was very slow or ceased for only a short period of time. A transition to porous columnar fabric after the “micro-hiatus” (i.e. above 9.35 mm DFT) is evident in the Ca map, with the tips of open columnar crystals clearly visible in the S, Sr and Mg maps. The development of open columnar fabric is consistent with rapid infiltration of supersaturated waters (Frisia et al., 2015). This evidence points to the dissolution of lime likely resulting from fire (discussed in further detail in Section 5.4), and the subsequent abrupt increase in vertical extension rate (Figure 3). The singular conspicuous peak in P in the LA-ICP-MS track (Figure 3) which reaches a maxima at 9.35 mm DFT is also evident in the synchrotron-generated P map in Figure 4 as a continuous lateral feature coincident with a depletion in S, and peak concentrations in Mg and Sr. This event appears to occur during the dry season, where the lamina in the thin section are lighter due to reduced colloid/OM incorporation (Figure S4).

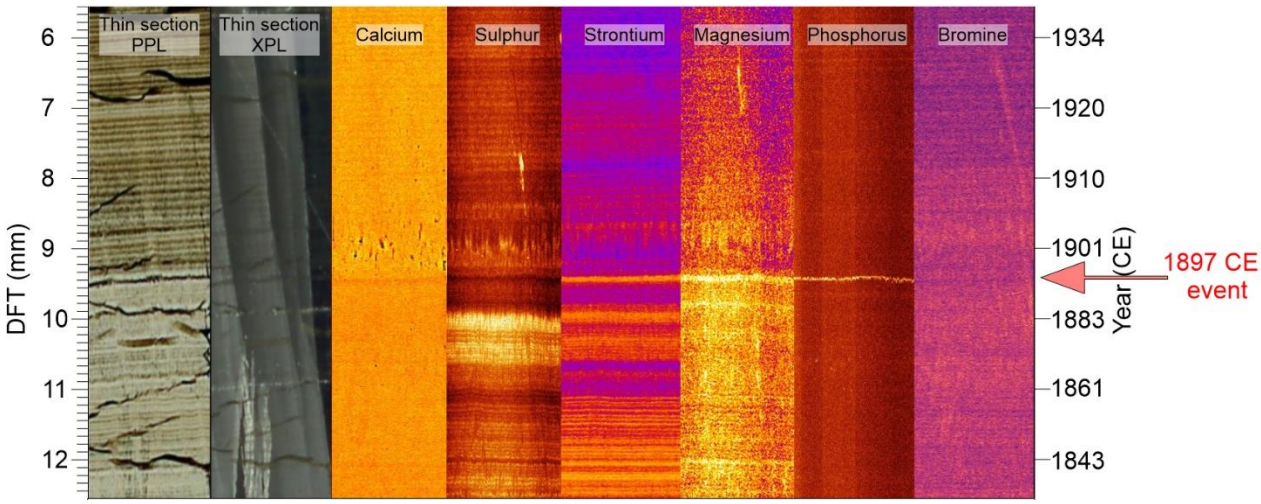

Figure 4: Thin section parallel-polar image (PPL), cross-polar image (XPL), and synchrotron XRF maps for calcium, sulphur, strontium, magnesium, phosphorus and bromine. The 1897 CE event is preceded by a micro-hiatus in the PPL image, a strong peak in P and smaller peaks in Mg and Sr. The post 1897 CE period is characterised by higher colloidal/OM

concentrations, a decline in Mg and Sr, and an increase in the calcite porosity evident in the Ca, Sr, S and Mg maps.

4.5 Principal Component Analysis

We undertook an initial PCA on the combined information from hydroclimate sensitive proxies to infer climatic conditions that lead to wildfires and obtain information about potential changes in water storage times, infiltration or flow paths brought about by fire. The results of the PCA are shown in Figure 5 and Table S4. PC1, PC2 and PC3 explain 46.7%, 19.2% and 8.8% of the variation in the dataset respectively.

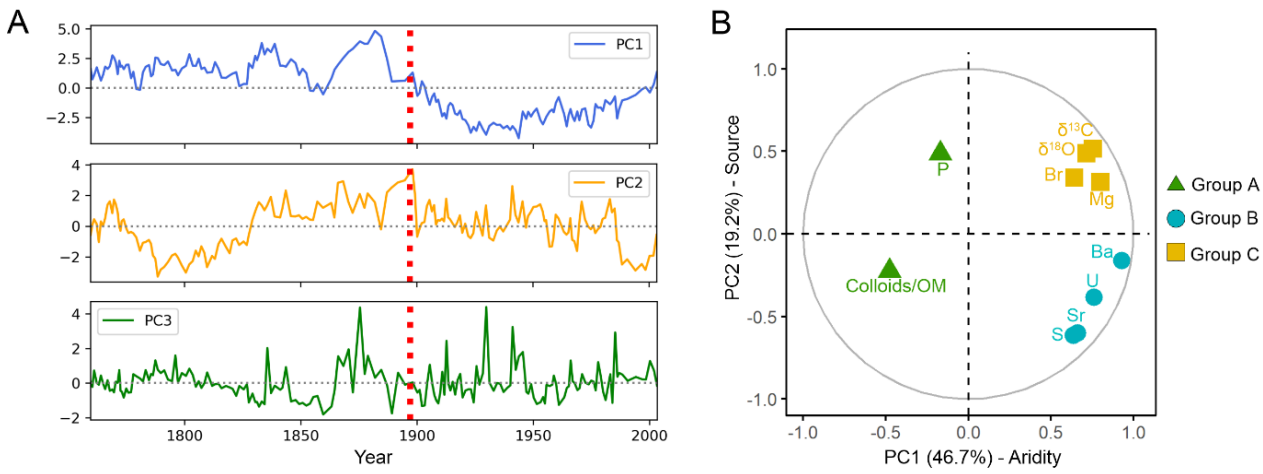

Figure 5: A) PCA time-series showing PC1 (blue), PC2 (yellow) and PC3 (green). The timing of the extreme event at 1897 CE is shown as red dashed line. B) PCA bi-plot showing three groupings of variables based on k-means (Table S5, between group sum of squares = 3.9). Note: data for 1897 CE have been removed from the analysis to decrease the influence of this one-off event on the PCA results.

4.5.1 PC1 and PC2 – Aridity and source components

Variables Mg, Ba, $\delta^{13}C$, $\delta^{18}O$, Br, U and colloids load most strongly on PC1 (Table S4), whereas S loads most strongly on PC2. The Sr loading is relatively evenly spread between PC1 and PC2, with P loading most strongly on PC3. PC1 represents a hydroclimate / aridity

component, reflecting changes in water-rock interactions (dissolution of host-rock and PCP) and salinity (evaporation and dilution). Parameters loading positively on PC1 (groups B and C in Figure 5) include elements derived from host-rock and aerosol inputs which decrease in concentration due to dilution or reduced water-rock interaction during periods of high meteoric precipitation or decreased evaporation. PC2 denotes the separation between soil (P) / aerosol (Br and Mg) elements and bedrock-derived elements This is supported by the expanded PCA shown in Figure S8 which includes soil-derived metals (Pb, Al, Cu and Zn) loading positively on PC2, opposite to Group B bedrock parameters.

Treble et al (2016) determined that the source of Mg and SO_4 are aerosols, while Sr was sourced from bedrock in dripwater at Golgotha Cave, a similar distance from the coast and similarly developed in the Tamala Limestone. Dripwater monitoring by Nagra et al. (2016) at two sites in Yonderup Cave show that Mg is correlated with Cl (R^2 = 0.82, n = 14 and R^2 = 0.76, n = 36), and additional Br data (Figure S6) are correlated with Cl (R^2 = 0.13, n = 14 and R^2 = 0.58, n= 36). The Cl:Br molar ratio in the dripwaters (0.00130) are close to that of sea water (0.00158), suggesting that Mg and Br are likely sourced from aerosols at Yonderup Cave also. Mg, $\delta^{13}C$ and $\delta^{18}O$ have previously been interpreted as proxies to distinguish wetter and drier conditions in south-west WA speleothems (Treble et al 2005) and the inclusion of Br in this group is consistent with this. PC1 also differentiates between the soil-derived parameters (OM/colloidal material and P) and bedrock-derived parameters, further supporting that this component represents aridity. Thus, PC1 describes the hydroclimate/aridity signal in this speleothem, with more bedrock and aerosol input under drier conditions as a result of evaporation, reduced water movement and increased water-rock interaction times resulting in higher PC1 values. This is supported by an increase in PC1 values after 1970 CE which is a known dry period for the region (Hope et al., 2010).

Overall, PC1 displays multi-decadal behavior with positive values observed prior to 1900 CE, suggesting drier conditions accompanied by increased aerosol and host-rock inputs during 1829 – 1845 CE and 1868 – 1887 CE (Figure 3). PC1 scores become negative after 1900

CE and continue to decline until approximately 1940 CE suggesting reduced water storage times and increased infiltration. After this time and particularly from about 1970 CE onwards, PC1 values begin to increase again up until the time of stalagmite retrieval, indicating increasingly dry conditions in the modern portion of the record. PC2 shows multi-decadal changes, with a notable increase from negative to positive values occurring in the 19th century, and a decline in PC2 values occurring after 1985 CE.

4.5.2 PC3 – Fire event component

PC3 shows high variability and largely represents pulses of P derived from soils (Figure 5) as represented by its strong loading on PC3 (Table S4). Peaks in PC3 were assessed to determine whether these align with known fire events in the modern record (as detailed in Section 2.2) and might assist in identification of fire events in the historical record. The original PCA shown in Figure 5 was re-run to include metals (Cu, Pb, Al and Zn) with all variables interpolated to high resolution LA-ICP-MS data (see Methods for more details). The biplot shown in Figure S8 confirms the soil source of these metals as they cluster with variables P and colloids/OM, which all load most strongly on PC3 in the updated PCA, and improve the percent variance explained by PC3 from 8.8% in the initial PCA, to 11.9%.

Peaks in PC3 are classified as values exceeding the rolling median PC3 value (window size = 40) by 2.5 times the rolling standard deviation. Figure 6 confirms that all known modern fire events are identified as peaks in PC3, aside from the 1983 CE event. Notably, the 1897 CE event is also clearly visible as a peak in PC3 in the historical record. Pb, Zn and Al load most strongly on PC3 (each explaining ≥ 15% of the variability on PC3) suggesting these parameters may be the most useful for identifying fire events.

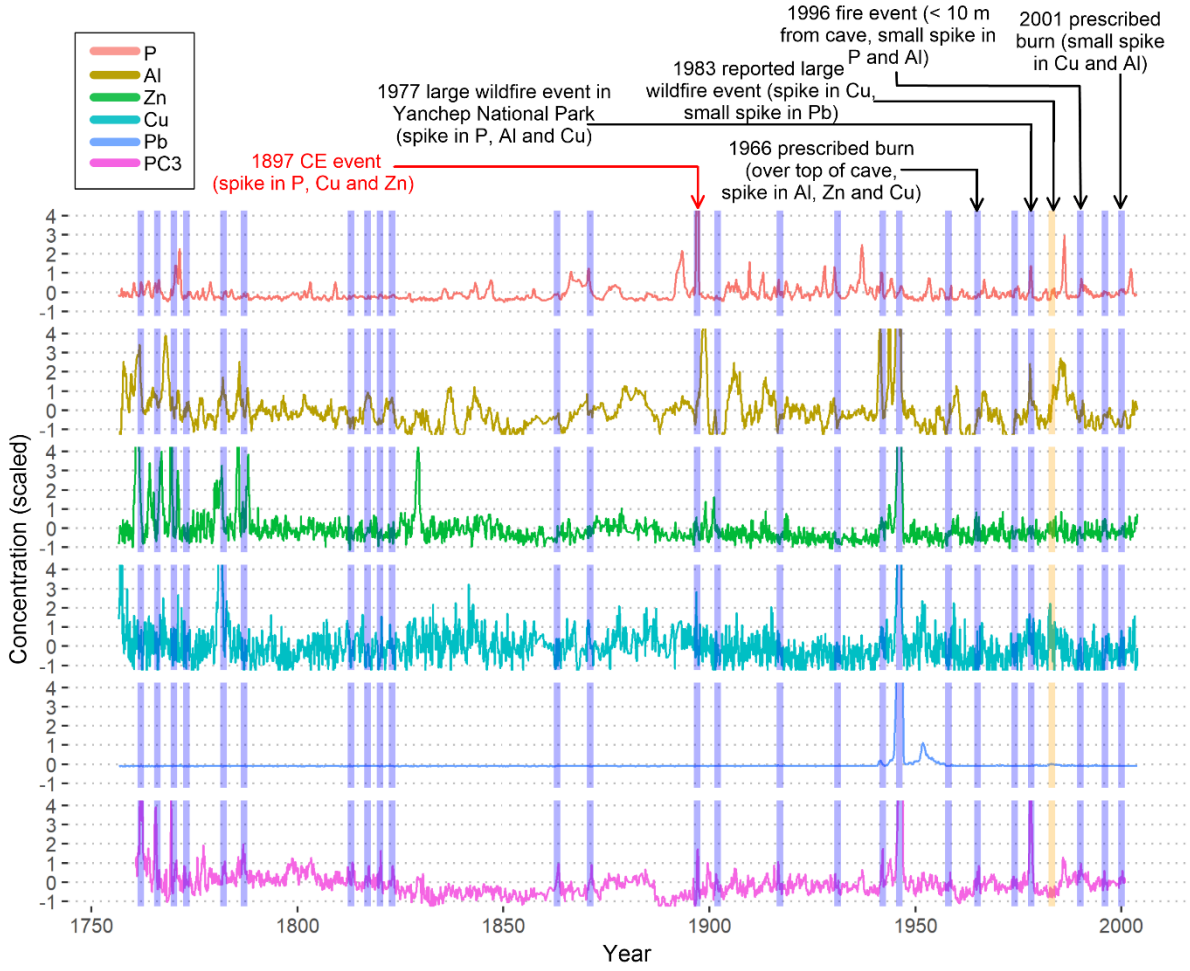

Figure 6: YD-S2 LA-ICP-MS time-series data of centred, scaled soil-derived metal (Cu, Al, Pb and Zn) and P concentrations, and PC3 time-series for the YD-S2 record (main plot). Data is centred and scaled by subtracting the mean and dividing by the standard deviation using the scale() function in RStudio. The y-axis limited to values between -1 and 4 for visual clarity. Blue bands represent points where the rolling median PC3 value exceeds 2.5 times the rolling standard deviation (window size = 40). The yellow band represents a period when another large fire has been reported to have occurred in Yanchep National Park (Department of Environment and Conservation, 2010). Fire extent maps are displayed in Supplementary Figure S1.

5 Discussion

5.1 Seasonal strontium and magnesium variability

Dripwaters which have undergone PCP have an altered chemistry which can be identified through a strong positive relationship (slope = 0.88–0.97) between ln(Sr/Ca) and ln(Mg/Ca) (Sinclair et al., 2012). Nagra et al (2016) show a strong PCP control (R^2 = 0.922 and 0.997, slope = 0.839 and 0.867 respectively) on seasonal dripwater Sr/Ca and Mg/Ca at YD-S2 and another drip site in Yonderup Cave. It was therefore interpreted that the seasonal Sr laminae in speleothem YD-S2 resulted from PCP. In contrast, we observe negative seasonal relationships between ln(Sr/Ca) and ln(Mg/Ca) through large portions of the YD-S2 stalagmite record (Figure S9), as has been documented in other speleothems from the region (e.g. MND-S1 in Treble et al., 2003). Mg concentrations and $\delta^{18}O$ values show a positive relationship in both the stalagmite and dripwater from YD-S2 (Nagra et al., 2016), as well as in MND-S1 (Treble et al., 2005), suggesting PCP controls dripwater and speleothem Mg/Ca concentrations. In contrast, Sr concentrations do not show seasonal variability in dripwater at YD-S2 (Nagra et al., 2016). This indicates that the antiphase relationship between *ln*(Mg/Ca) and *ln*(Sr/Ca) through most of the YD-S2 record (Figure S9) must arise during the incorporation of Sr into the speleothem calcite. The mechanism for this is unclear, however as Sr irreversibly binds to low molecular weight organic molecules (Boyer et al., 2018), it is possible that in the wet season Sr may be preferentially bound to low molecular weight organics whilst higher molecular weight organics which are not bound to Sr may be preferentially incorporated into the speleothem.

5.2 Fire record in YD-S2

5.2.1 Response to known fire events

An examination of the time-series data in Figure 6 reveals that whilst PC3 displays short term peaks at most known modern fire events (e.g. 1966 CE, 1977 CE, 1983 CE, 1996 CE, and 2001 CE), the combination of elements that simultaneously increase varies. For example, a peak in PC3 values is observed around 1966 CE when a prescribed burn took place over the cave. The peak in PC3 at this time appears to be due to a small increase in Al, Zn and Cu, and is closely followed by a spike in P the following year (9.2 ppm). The peak

in P represents the highest concentration in 13 years prior, since 1953 CE. It also represents the highest P peak until the known wildfire in 1977 CE (Department of Environment and Conservation, 2010). By contrast, the 1977 CE peak in PC3 is due to increases in P, Al and Cu (Figure 6), with the 1977 CE annual averages of P exceeding the 80th percentile of all data (Table S6). This event shows no apparent response in Zn. Nagra et al. (2017) previously attributed this increase being the result of a heavy rainfall event in 1974 CE, however our improved chronology places this event at the time of the reported fire in YNP.

The 1983 CE YNP fire event (Department of Environment and Conservation, 2010) is the only known modern event that does not appear as a peak in PC3. As the fire did not pass over the top of the cave (Figure S1), it is possible that significant ash deposition may not have occurred at the surface above YD-S2, particularly if the prevailing wind conditions at the time did not direct air-borne ash towards the cave.

A small peak in PC3 is observed during the prescribed burn in 2001 CE, where there is a small increase in Al (Figure 6). This suggests that the response to this fire is minor, consistent with the small burn extent for this fire event as shown in Figure S1. The 2005 CE wildfire which occurred over the top of the cave on January 6th, just over 6 months prior to the stalagmite retrieval, does not show up as increases in metals (Figure 6) at the end of the record, and suggests that ash from a large fire (Figure S1) may have taken over 6 months before it is incorporated into YD-S2. A number of additional peaks in P are evident in Figure 6, however, these do not show up as peaks in PC3 and are not accompanied by significant peaks in transition metals.

5.2.2 Paleo-fire events

The YD-S2 record through recent decades permits validation of short-term peaks in P and Al, Zn, Cu and Pb as indicators of fire events. Figure 6 also shows peaks in PC3 in the YD-S2 record prior to the 1966 CE fire record. These peaks indicate possible fires also occurred in the years 1762 CE, 1766 CE, 1769 CE, 1773 CE, 1782 CE, 1787 CE, 1813 CE, 1817 CE,

1820 CE, 1823 CE, 1863 CE, 1871 CE, 1897 CE, 1902 CE, 1917 CE, 1931 CE, 1942 CE, 1946 CE and 1958 CE. Each of these peaks is associated with a spike in Zn, Al, Cu, Pb or P. It is noted however that the height of the PC3 peak may not be representative of the fire intensity. For example, moderate intensity events could result in particularly high PC3 peaks if the burn temperature is not hot enough to result in volatilisation of elements. Alternatively, volatilisation of elements during extremely high intensity events, and less ash created during low intensity events could both potentially result in lower PC3 peaks, suggesting that this geochemical technique may be most useful for identification of moderate intensity or large-scale fire events. It is also noted that the spatial distribution of different trace metals in ash varies depending on the vegetation species within that local catchment and the microtopography of the soil (Pereira and Úbeda, 2010), likely resulting in further differences in trace metal composition of dripwater after wildfires. In addition, some dripwater metals may have an OM bound soil source (Hartland et al, 2012) as well as a vegetation source, which is not differentiated by the PCA. Finally, hydrology likely has an impact on the concentration and incorporation of trace metals into dripwater, which may make the fire signal recorded in the speleothem inconsistent between events. For example, a single large recharge event following a fire may flush the ash through the system resulting in some dilution of the ash leachate.

The highest P concentration (161 ppm) in the record is observed in 1897 CE. Aside from this event, P concentrations during identified peaks in PC3 are significantly lower ($p = 0.02$) and less variable (average = 4.0, variance = 1.9, n = 10) in the pre-1850 CE period than in the post-1900 CE period (mean = 6.3, variance = 11.5, n = 12). This is consistent with reports of Indigenous Australian land management as involving frequent low intensity fires to promote plant regrowth and attract game animals for hunting (Hallam, 2014). Historical records indicate that the Noongar people continued this practice until approximately 1830 –1860 CE, after which cultural burning was supressed (Abbott, 2002; Hallam, 2014). It is noted that

other factors such as climate could also affect PC3 peak identifications pre- and post-European settlement.

5.2.3 The 1897 CE fire

From approximately 1886 CE, PC1 and elements U, S and Ba show a sharp decline (Figure 3 and Figure 5). A comparison of the weight ratios of *log*(Sr/Ca) and *log*(Mg/Ca) shows a negative correlation for most of the time-series, with slopes of between -0.14 and -0.66 (Figure S9). However, during short time intervals such as the six year period prior to the 1897 CE event, YD-S2 is characterized by high Mg, $\delta^{18}O$ and $\delta^{13}C$ values, and a positive relationship (R^2 = 0.89, slope = 0.347) between ln(Sr/Ca) and ln(Mg/Ca) (Figure S9). This suggests a short period of PCP, whereby the PCP signal overrides the seasonal signal that otherwise dominates and results in the negative correlation of Sr/Ca and Mg/Ca in the rest of the record. It is likely that this period of enhanced PCP, coinciding with high $\delta^{18}O$ and $\delta^{13}C$ values, was caused by the Australian Federation Drought (Godfree et al., 2019). This drought affected much of Australia between 1895 CE and 1902 CE. Reconstructed rainfall rates for the Southern and South Western Flatlands for the period show that the drought affected the area encompassing YNP (Freund et al., 2017). This dry period would result in ideal conditions under which an extreme fire could occur. Peaks in PC3 in the reconstructed record (Figure 6) confirm that the 1897 CE event was a likely fire event coinciding with the timing of this drought. Figure 3 and Figure 4 highlight that the 1897 CE fire was an unusually extreme event in the last two centuries of YD-S2's growth history that affected the karst water balance, speleothem crystal fabric, extension rate and also pulse-concentration of metals associated with ash and/or soil. It also occurs several decades after cultural burning by Indigenous Australians is thought to have ceased. Thus, it is also possible that this permitted an increase in fuel load to build up on the forest floor and that this further contributed to the intensity of the fire event inferred from the geochemical record.

The changes observed in YD-S2 in 1897 CE are consistent with a flushing of metal-bearing ash, colloidal particulate and associated adsorbed metals into dripwater. A study conducted after the Cerro Grande fire in 2000 in New Mexico reported that metals were mostly associated with ash-derived particulate fraction and not present as dissolved species in water (Cerrato et al., 2016). Thus, it is likely that ash-derived particulate and phosphate molecules temporarily poisoned growth sites at calcite crystal surfaces (Dove et al., 1993; Lin and Singer, 2005). Short-term spikes in parameters Mg are also evident in the record at 1897 CE (Figure 3) consistent with the short period of PCP identified Figure S9. A drop in S concentrations is also observed at the timing of the event (Figure 4) suggesting soil S was volatilised during the fire. In some locations where dripwater S is largely derived from vegetation, S may become source-limited for a prolonged period post-fire due to the removal of overlying vegetation (Treble et al., 2016). The opposite loadings of S compared to aerosol-sourced Mg and Br suggests that the predominant source of S in YD-S2 is derived from the bedrock and is a possible explanation of why it is not source-limited in this case.

A short-term peak in $\delta^{18}O$ is observed during the 1897 CE fire. Nagra et al. (2016) previously identified an increase in dripwater $\delta^{18}O$ of approximately 2‰ and concentration of ions after the 2005 CE fire which burned above Yonderup Cave just prior to the removal of YD-S2. This increase was observed for > 5 years after the 2005 CE fire event at another drip site in Yonderup Cave and was therefore attributed to a reduction of canopy cover and albedo causing increased evaporation and a subsequent concentration of ions. In contrast, the 1897 CE fire led to an initial increase, followed by a steep decline in $\delta^{18}O$ values which suggests a short period of evaporative concentration caused by heat from the fire (Bian et al., 2019) counteracted by a change in karst hydrology shortly after, as outlined below.

5.2.4 Changes in surface-cave hydrology and climate after the 1897 CE fire

The prolonged decline in $\delta^{18}O$ values after the 1897 CE wildfire event suggests an increase in rainfall infiltration, likely coinciding with a reduction in evaporation and evapotranspiration

due to decreased water storage and vegetation cover. We propose that the heating of the limestone also resulted in increased meso- and macro-porosity which resulted in faster transmission of rainfall into the aquifer, reduced water storage times, and is consistent with the increased colloid/OM incorporation observed in YD-S2 (Figure 3, see also the dark banding post-1897 CE in Figure 4). OM particulate in speleothems has been commonly ascribed as originating in the soil/surface zone and can be adsorbed at calcite crystal surfaces, thus marking their tips during speleothem growth as determined by both optical and fluorescent layers (Baker et al., 2008). When OM is dissolved in the water, it is most likely incorporated within the crystals to yield pervasive fluorescence (Ramseyer et al., 1997). Our observation of increased adsorption of OM particulate onto the speleothem post-fire may be the result of reduced physical filtering of OM colloids due to increased porosity and ash-related abundance of OM compounds. Furthermore, localised lime formation in the upper epikarst due to the high temperatures, and subsequent dissolution into dripwaters could have resulted in an increase in alkalinity and supersaturation, enhancing speleothem growth rate (Figure 3).

The decline in PC1 observed after the 1897 CE fire event indicates an overall dilution effect enhanced by the increase in karst porosity post-fire. Some parameters including Mg and $\delta^{13}C$ show an initial increase and then step decline in concentrations after 1897 CE, suggesting that they are heavily impacted by evaporation during the intense heat of the fire as well as subsequent reduction in water-rock interaction or dilution caused by a sudden increase in host rock porosity post-fire. Other elements such as Br slowly decline between approximately 1900 CE – 1960 CE. This period has been identified from instrumental data as being relatively wetter in south-west WA as identified by breakpoints in rainfall timeseries data for the region (Hope et al., 2009). This is supported by the lower $\delta^{18}O$ values through this period which indicate that larger rainfall events impact in the region at this time. The lower $\delta^{18}O$ values are also likely enhanced by increased bedrock porosity or fracture type flow. The decline in PC1 in the early to mid-1900s CE therefore appears to reflect a mixed

signal of dilution caused by increased rainfall and decreased water-rock interaction resulting from changed bedrock hydrology. As noted in Section 4.5.1, Br is likely sourced from aerosols at this site and is consistent with behaving as a conservative element, mainly affected by dilution. Br sourced from soil OM or ash has previously been reported (Kabata-Pendias, 2010; Wang et al., 2015), however this is unlikely here given that the post-1897 CE decline in Br is associated with an increase in OM, and because Br loads negatively on PC3, opposite to the ash-derived metals, P and OM.

Changes in hydrology post-1897 CE fire, and its impacts on dripwater chemistry and speleothem growth are summarised in Figure 7.

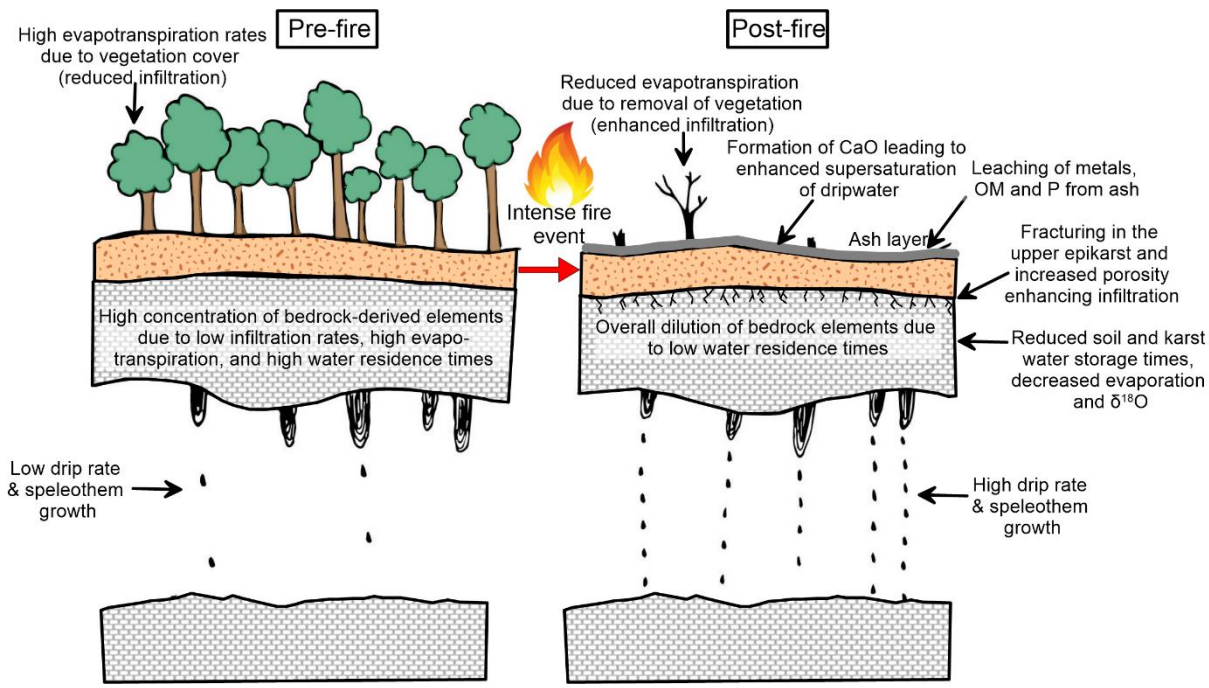

Figure 7: Conceptual figure showing the impacts of fire on stalagmite YD-S2. The reduction in vegetation cover post-fire results in reduced evapotranspiration and subsequent increased infiltration of precipitation into the bedrock which is further enhanced by fracturing of the upper epikarst. Overall, bedrock and aerosol-derived parameters are reduced due to dilution and reduced water residence times resulting from enhanced meso- and macro-porosity. The combustion of vegetation results in an ash layer containing OM, P and metals which are leached into the subsurface and incorporated into the speleothem.

6 Conclusions

This study utilises a large suite of analyses including stable isotopes ($\delta^{13}C$, $\delta^{18}O$), elemental and organic matter concentrations, as well as a thorough understanding of the karst hydrology, to establish a combined fire and climate record for the study site. We provide a novel demonstration of the ability to pinpoint the timing of palaeo-fire events, particularly when they form in shallow cave settings. Our results reveal that in Yonderup Cave, particularly intense wildfires may translate into speleothems as increases in ash-derived elements such as P, Al and Cu coupled with maxima in $\delta^{13}C$ and Mg, and short-term increases in $\delta^{18}O$ after evaporative enrichment. In contrast, lower intensity fires may appear as pulses in different combinations of metals (Cu, Pb, Al, Zn) and P, and may not be associated with obvious increases in bedrock-derived elements. Traditional suites of bedrock-derived elements (Mg, Sr, Ba) therefore do not appear to be reliable indicators of fire alone. Rather, these elements are useful for interpreting climate leading up to a fire event, as well as PCP and changes in hydrology post-fire.

Using the geochemical proxies considered here, we interpret that the period from 1760 CE until approximately 1825 CE is a period characterised by low intensity, high frequency fire events in the region. There are two possible drier periods between the 1820's – 1850's CE and 1860's – 1890's CE. The latter is in the instrumental record and coincides with the Federation Drought. The YD-S2 record shows that this dry period resulted in an enhanced PCP signal and culminated in a significant fire in 1897 ± 5 CE. The intensity of the fire is likely to have been exacerbated by dry conditions, but possibly also due to a transition away from cultural burning practices by Indigenous Australia which may have resulted in fuel build-up.

Decreases in proxies $\delta^{18}O$, $\delta^{13}C$, Ba, U, Sr, S, Br and Mg after the 1897 CE fire event indicate a transition to wetter conditions, however, we also present evidence for a significant change in karst hydrology caused by heat from the fire event that likely intensified the shift in

these proxies. The decrease in Br during this period demonstrates its applicability for use as a water balance proxy, and suggests that it may be particularly useful at sites within close proximity to the coastline due to its apparent aerosol source. The decline in water-rock interaction resulting from changes in the bedrock hydrology post-fire demonstrates how a paleoclimate interpretation could be exaggerated without taking into account the impact of fire on this record. Fire events may result in an increase in OM flushed through fractures or widened pores, which could also be misinterpreted as higher amounts of surface vegetation. These findings are particularly relevant for palaeoclimate studies of shallow caves in water-limited environments with thin soil profiles where the impact of fire events should be taken into account.

Acknowledgements: The authors thank Alan Griffiths from ANSTO for the PCA Python and general advice regarding coding in Python, Stuart Hankin from ANSTO for providing the 1983 CE imagery shown in Figure S1, and Martin de Jonge for assistance with Melbourne Synchrotron scans. Thanks to the staff at Yanchep National Park who assisted with fieldwork. Stalagmite YD-S2 was collected under permit obtained from Parks and Wildlife Service. We also thank Susan Dalgleish from the City of Wanneroo, Ursula Salmon from SA Department of Water and Environmental Regulation, Derek Nannup for general discussion regarding the site, Joe Dortch from the University of Western Australia for manuscript comments, and Janine Kinloch from the Department of Biodiversity, Conservation and Attraction for providing spatial information regarding modern fire frequency and extent for the region. The authors would like to respectfully acknowledge the Whadjuk Noongar people, the traditional custodians of the land at Yanchep where this study was conducted, for whom the land has strong mythological, ritual and ceremonial significance.

Author contributions: Funding for the project was obtained by P.C.A and A. Baker. Manuscript drafting, data pre-processing and figure generation was undertaken by L.K.M. under the guidance of P.C.T. and A. Baker. P.C.T. prepared thin and thick sections and carried out the LA-ICPMS analyses. P.C.T prepared samples for stable isotope analysis and

the measurements were carried out while M.K.G. was at RSES, ANU, with the technical support of Joe Cali, Heather Scott-Gagan and Joan Cowley. M.K.G. also provided comments on the manuscript. P.C.T., A. Borsato, K.C., D.P. and S.C.F. performed Synchrotron scans and provided manuscript comments. S.C.F. processed the Advanced Light Source synchrotron scans. A. Borsato generated thin section scans, provided guidance on data processing and contributed to the interpretations of the data. S. Frisia., G.N. and U.S. contributed to the interpretation of the data and provided comments on the manuscript.

Funding: This work was partially funded through the Australian Research Council *Discovery* Project DP200100203. Access to the Australian Synchrotron was under experiment 13457. Access to the Advanced Light Source synchrotron was under experiment ALS-10166. We acknowledge travel funding provided by the International Synchrotron Access Program (ISAP) managed by the Australian Synchrotron, part of ANSTO, and funded by the Australian Government. This research used resources of the Advanced Light Source, a U.S. DOE Office of Science User Facility under contract no. DE-AC02-05CH11231.

Data availability: Data is available upon request to the corresponding author.

References

1. Baker, A., Smith, C.L., Jex, C., Fairchild, I.J., Genty, D. and Fuller, L. (2008) Annualy laminated speleothems: a review. *International Journal of Speleology* **37**, 193-206.
2. Bar-Matthews, M., Ayalon, A. and Kaufman, A. (1997) Late Quaternary paleoclimate in the Eastern Mediterranean region from stable isotope analysis of speleothems at Soreq Cave, Israel. *Quaternary Research* **47**, 155-168.
3. Beard, J.S., Beeston, G.R., Harvey, J., Hopkins, A.J.M. and Shepherd, D.P. (2013) The vegetation of Western Australia at the 1:3,000,000 scale. Explanatory memoir. Second edition. *Conservation Science Western Australia* **9**, 1-152.
4. Belli, R., Borsato, A., Frisia, S., Drysdale, R., Maas, R. and Greig, A. (2017) Investigating the hydrological significance of stalagmite geochemistry (Mg, Sr) using

Sr isotope and particulate element records across the Late Glacial-to-Holocene transition. *Geochimica et Cosmochimica Acta* **199**, 247-263.

5. Bian, F., Coleborn, K., Flemons, I., Baker, A., Treble, P.C., Hughes, C.E., Baker, A., Andersen, M.S., Tozer, M.G., Duan, W., Fogwill, C.J. and Fairchild, I.J. (2019) Hydrological and geochemical responses of fire in a shallow cave system. *Science of the Total Environment* **662**, 180-191.
6. Bodí, M.B., Martin, D.A., Balfour, V.N., Santín, C., Doerr, S.H., Pereira, P., Cerdà, A. and Mataix-Solera, J. (2014) Wildland fire ash: Production, composition and eco-hydro-geomorphic effects. *Earth-Science Reviews* **130**, 103-127.
7. Boyer, A., Ning, P., Killey, D., Klukas, M., Rowan, D., Simpson, A. J. and Passeport, E. (2018) Strontium adsorption and desorption in wetlands: Role of organic matter functional groups and environmental implications. *Water Research* **133**, 27-36.
8. Abbott, I. (2002). *Historical records of Noongar fires, 1658-1888 : a compendium*. Dept. of Conservation & Land Management, Kensington, W.A.
9. Butler, O.M., Elser, J.J., Lewis, T., Mackey, B. and Chen, C. (2018) The phosphorus-rich signature of fire in the soil–plant system: a global meta-analysis. *Ecology Letters* **21**, 335-344.
10. Cerrato, J.M., Blake, J.M., Hirani, C., Clark, A.L., Ali, A.M., Artyushkova, K., Peterson, E. and Bixby, R.J. (2016) Wildfires and water chemistry: effect of metals associated with wood ash. *Environmental Science: Processes & Impacts* **8**, 1078-89.
11. Certini, G. (2005) Effects of fire on properties of forest soils: a review. *Oecologia* **143**, 1-10.
12. Cheng, H., Spötl, C., Breitenbach, S.F.M., Sinha, A., Wassenburg, J.A., Jochum, K.P., Scholz, D., Li, X., Yi, L., Peng, Y., Lv, Y., Zhang, P., Votintseva, A., Loginov, V., Ning, Y., Kathayat, G. and Edwards, R.L. (2016) Climate variations of Central Asia on orbital to millennial timescales. *Scientific Reports* **6**, 36975.
13. Coleborn, K., Spate, A., Tozer, M., Andersen, M.S., Fairchild, I.J., MacKenzie, B., Treble, P.C., Meehan, S., Baker, A. and Baker, A. (2016) Effects of wildfire on long-

term soil CO_2 concentration: implications for karst processes. *Environmental Earth Sciences* **75**, 330, https://doi.org/10.1007/s12665-015-4874-9.

14. DeBano, L.F. (2000) The role of fire and soil heating on water repellency in wildland environments: a review. *Journal of Hydrology* **231-232**, 195-206.
15. Department of Conservation and Land Management (CALM). (1989). *Yanchep National Park Management Plan 1989-1999*. Como, Western Australia.
16. Department of Environment and Conservation (2010) Parks and Reserves of Yanchep and Neerabup Draft Management Plan 2010. Available at https://library.dbca.wa.gov.au/static/FullTextFiles/025376.pdf. Retrieved January 15, 2021.
17. Dorale, J.A., Edwards, R.L., Ito, E., Gonzalez, L.A. (1998) Climate and vegetation history of the midcontinent from 75 to 25 ka: a speleothem record from Crevice Cave, Missouri, USA. *Science* **282**, 1871-1874.
18. Dove, P.M. and Hochella Jr, M.F. (1993) Calcite precipitation mechanisms and inhibition by orthophosphate: In situ observations by Scanning Force Microscopy. *Geochimica et Cosmochimica Acta* **57**, 705-714.
19. Faraji, M., Borsato, A., Frisia, S., Hellstrom, J., Lorrey, A., Hartland, A., Greig, A. and Mattey, D.P. (2021) Accurate dating of stalagmites from low seasonal contrast tropical Pacific climate using Sr 2D maps, fabrics and annual hydrological cycles. *Scientific Reports* **11**, https://doi.org/10.1038/s41598-021-81941-x.
20. Freund, M., Henley, B.J., Karoly, D.J., Allen, K.J. and Baker, P.J. (2017) Multi-century cool- and warm-season rainfall reconstructions for Australia's major climatic regions. *Climates of the Past* **13**, 1751-1770.
21. Frisia, S. (2015) Microstratigraphic logging of calcite fabrics in speleothems as tool for palaeoclimate studies. International Journal of Speleology **44**, 1-16.
22. Frisia, S., and Borsato, A. (2010) Karst, in Alonso-Zarza A.M. and Tanner L.H. (Eds.) *Developments in Sedimentology*. Elsevier, pp. 269-318.

23. Gagan, M.K., Chivas, A.R. and Isdale, P.J. (1994) High-resolution isotopic records from corals using ocean temperature and mass-spawning chronometers. *Earth and Planetary Science Letters* **121**, 549-558.

24. Genty, D. and Quinif, Y. (1996) Annually laminated sequences in the internal structure of some Belgian stalagmites; importance for paleoclimatology. *Journal of Sedimentary Research* **66**, 275-288.

25. Godfree, R.C., Knerr, N., Godfree, D., Busby, J., Robertson, B. and Encinas-Viso, F. (2019) Historical reconstruction unveils the risk of mass mortality and ecosystem collapse during pancontinental megadrought. *Proceedings of the National Academy of Sciences* **116**, 15580.

26. Grove, T.S., O'Connell, A.M., Dimmock, G.M. (1986) Nutrient changes in surface soils after an intense fire in jarrah (*Eucalyptus marginata* Donn ex Sm.) forest. *Australian Journal of Ecology* **11**, 303-317.

27. Hallam , S.J. (2014) *Fire and Hearth a study of Aboriginal usage and European usurpation in south-western Australia*. Revised Edition. UWA Publishing, Crawley, Western Australia.

28. Harper, A.R., Santin, C., Doerr, S.H., Froyd, C.A., Albini, D., Otero, X.L., Viñas, L. and Pérez-Fernández, B. (2019) Chemical composition of wildfire ash produced in contrasting ecosystems and its toxicity to *Daphnia magna*. I*nternational Journal of Wildland Fire* **28**, 726-737.

29. Hartland, A., Fairchild, I., Lead, J., Dominguez-Villar, D., Baker, A., Gunn, J., Baalousha, M., Ju-Nam, Y. and Ju-Nam, Y.K. (2010) The dripwaters and speleothems of Poole's Cavern: a review of recent and ongoing research. *Cave and Karst Science* **36**, 37-46.

30. Hartland, A., Fairchild, I.J., Lead, J.R., Borsato, A., Baker, A., Frisia, S. and Baalousha, M. (2012) From soil to cave: transport of trace metals by natural organic matter in karst dripwaters. *Chemical Geology* **304-305**, 68-82.

31. Hellstrom, J., McCulloch, M. and Stone, J. (1998) A Detailed 31,000-Year Record of Climate and Vegetation Change, from the Isotope Geochemistry of Two New Zealand Speleothems. *Quaternary Research* **50**, 167-178.
32. Heydari, M., Rostamy, A., Najafi, F. and Dey, D.C. (2017) Effect of fire severity on physical and biochemical soil properties in Zagros oak (Quercus brantii Lindl.) forests in Iran. *Journal of Forestry Research* **28**, 95-104.
33. Hogue, B.A. and Inglett, P.W. (2012) Nutrient release from combustion residues of two contrasting herbaceous vegetation types. *Science of the Total Environment* **431**, 9-19.
34. Hope, P., Timbal, B. and Fawcett, R. (2010) Associations between rainfall variability in the southwest and southeast of Australia and their evolution through time. *International Journal of Climatology* **30**, 1360-1371.
35. Hopley, P.J., Marshall, J.D., Weedon, G.P., Latham, A.G., Herries, A.I., Kuykendall, K.L. (2007) Orbital forcing and the spread of C4 grasses in the late Neogene: stable isotope evidence from South African speleothems. *Journal of Human Evolution* **53**, 620-634.
36. Kabata-Pendias, A. (2010) *Trace Elements in Soils and Plants*. Fourth edition. CRC Press, Boca Raton, FL.
37. Kassambara, A. and Mundt, F. (2020) Factoextra: extract and visualise the results of multivariate data analyses. R package v1.0.7. https://CRAN.R-project.org/package=factoextra.
38. Kemperl, J. and Maček, J. (2009) Precipitation of calcium carbonate from hydrated lime of variable reactivity, granulation and optical properties. *International Journal of Mineral Processing* **93**, 84-88.
39. Killick, R., Fearnhead, P. and Eckley, I.A. (2012) Optimal detection of changepoints with a linear computational cost. *Journal of the American Statistical Association* **107**, 1590–1598.

40. Lasanta, T. and Cerdà, A. (2005) Long-term erosional responses after fire in the Central Spanish Pyrenees: 2. Solute release. *CATENA* **60**, 81-100.
41. Lê, S., Josse, J. and Husson, F. (2008) FactoMineR: an R package for multivariate analysis. *Journal of Statistical Software* **25**, 18.
42. Lin, Y.P. and Singer, P.C. (2005) Inhibition of calcite crystal growth by polyphosphates. *Water Research* **39**, 4835-4843.
43. Lipar, M. and Webb, J.A. (2014) Middle–late Pleistocene and Holocene chronostratigraphy and climate history of the Tamala Limestone, Cooloongup and Safety Bay Sands, Nambung National Park, southwestern Western Australia. *Australian Journal of Earth Sciences* **61**, 1023-1039.
44. Marcus, M.A., MacDowell, A.A., Celestre, R., Manceau, A., Miller, T., Padmore, H.A. and Sublett, R.E. (2004) Beamline 10.3.2 at ALS: a hard X-ray microprobe for environmental and materials sciences. *Journal of Synchrotron Radiation* **11**, 239-147.
45. Mast, M.A. and Clow, D.W. (2008) Effects of 2003 wildfires on stream chemistry in Glacier National Park, Montana. *Hydrological Processes* **22**, 5013-5023.
46. Mayer, B., Fritz, P., Prietzel, J. and Krouse, H.R. (1995) The use of stable sulfur and oxygen isotope ratios for interpreting the mobility of sulfate in aerobic forest soils. *Applied Geochemistry* **10**, 161-173.
47. McCaw, W.L., and Hanstrum, B. (2003) Fire environment of Mediterranean south-west Western Australia, in I Abbott and N Burrows eds., *Fire in ecosystems of south-west Western Australia: impacts and management*. Backhuys Publishers, Leiden, The Netherlands, p. 87-106.
48. Meng, Q.-B., Wang, C.-K., Liu, J.-F., Zhang, M.-W., Lu, M.-M. and Wu, Y. (2020) Physical and micro-structural characteristics of limestone after high temperature exposure. *Bulletin of Engineering Geology and the Environment* **79**, 1259-1274.
49. Moreira, F., Ascoli, D., Safford, H., Adams, M.A., Moreno, J.M., Pereira, J.M.C., Catry, F.X., Armesto, J., Bond, W., González, M.E., Curt, T., Koutsias, N., McCaw, L., Price, O., Pausas, J.G., Rigolot, E., Stephens, S., Tavsanoglu, C., Vallejo, V.R.,

Van Wilgen, B.W., Xanthopoulos, G. and Fernandes, P.M. (2020) Wildfire management in Mediterranean-type regions: paradigm change needed. *Environmental Research Letters* **15**, 011001.

50. Moropoulou, A., Bakolas, A. and Aggelakopoulou, E. (2001) The effects of limestone characteristics and calcination temperature to the reactivity of the quicklime. *Cement and Concrete Research* **31**, 633-639.
51. Nagra, G., Treble, P.C., Andersen, M.S., Bajo, P., Hellstrom, J. and Baker, A. (2017) Dating stalagmites in mediterranean climates using annual trace element cycles. *Scientific Reports* **7**, https://doi.org/10.1038/s41598-017-00474-4.
52. Nagra, G., Treble, P.C., Andersen, M.S., Fairchild, I.J., Coleborn, K. and Baker, A. (2016) A post-wildfire response in cave dripwater chemistry. *Hydrology and Earth System Science* **20**, 2745-2758.
53. Pereira, P. and Úbeda, X. (2010) Spatial distribution of heavy metals released from ashes after a wildfire. *Journal of Environmental Engineering and Landscape Management* **18**, 13-22.
54. Petticrew, E.L., Owens, P.N. and Giles, T.R. (2006) Wildfire Effects on the Quantity and Composition of Suspended and Gravel-Stored Sediments, in: Kronvang, B., Faganeli, J., Ogrinc, N. (Eds.), *The Interactions Between Sediments and Water*. Springer Netherlands, Dordrecht, pp. 283-292.
55. Playford, P.E., Cockbain, A.E. and Low, G.H. (1976) Geology of the Perth Basin Western Australia. Geological Survey of Western Australia, Bulletin 124.
56. Playford, P.E., Cockbain, A.E., Berry, P.F., Roberts, A.P., Haines, P.W., and Brooke, B.P. (2013) Geology of Shark Bay. Geological Survey of Western Australia, Bulletin 146.
57. Plumlee, G.S., Martin, D.A., Hoefen, T., Kokaly, R., Hageman, P., Eckberg, A., Meeker, G.P., Adams, M., Anthony, M. and Lamothe, P.J. (2007) Preliminary Analytical Results for Ash and Burned Soils from the October 2007 Southern

California Wildfires: U.S. Geological Survey Open-File Report 2007–1407. U.S. Geological Survey, Reston, Virginia.

58. Quigley, K.M., Wildt, R.E., Sturtevant, B.R., Kolka, R.K., Dickinson, M.B., Kern, C.C., Donner, D.M. and Miesel, J.R. (2019) Fuels, vegetation, and prescribed fire dynamics influence ash production and characteristics in a diverse landscape under active pine barrens restoration. *Fire Ecology* **15**, https://doi.org/10.1186/s42408-018-0015-7.
59. Ramseyer, K., Miano, T.M., D'Orazio, V., Wildberger, A., Wagner, T. and Geister, J. (1997) Nature and origin of organic matter in carbonates from speleothems, marine cements and coral skeletons. *Organic Geochemistry* **26**, 361-378.
60. Revchuk, A.D. and Suffet, I.H. (2014) Effect of Wildfires on Physicochemical Changes of Watershed Dissolved Organic Matter. *Water Environment Research* **86**, 372-381.
61. Ryan, C.G., Etschmann, B.E., Vogt, S., Maser, J., Harland, C.L., van Achterbergh, E. and Legnini, D. (2005) Nuclear microprobe – synchrotron synergy: Towards integrated quantitative real-time elemental imaging using PIXE and SXRF. *Nuclear Instruments and Methods in Physics Research Section B: Beam Interactions with Materials and Atoms* **231**, 183-188.
62. Ryan, C.G., Jamieson, D.N., Churms, C.L. and Pilcher, J.V. (1995) A new method for on-line true-elemental imaging using PIXE and the proton microprobe. *Nuclear Instruments and Methods in Physics Research Section B: Beam Interactions with Materials and Atoms* **104**, 157-165.
63. Ryan, S.E., Dwire, K.A. and Dixon, M.K. (2011) Impacts of wildfire on runoff and sediment loads at Little Granite Creek, western Wyoming. *Geomorphology* **129**, 113-130.
64. Savage, S.M. (1974) Mechanism of Fire-Induced Water Repellency in Soil. *Soil Science Society of America Journal* **38**, 652-657.

65. Schaller, J., Tischer, A., Struyf, E., Bremer, M., Belmonte, D.U. and Potthast, K. (2015) Fire enhances phosphorus availability in topsoils depending on binding properties. *Ecology* **96**, 1598-1606.

66. Scott, A.J. and Knott, M. (1974) A cluster analysis method for grouping means in the analysis of variance. *Biometrics* **30**, 507-512.

67. Sinclair, D.J., Banner, J.L., Taylor, F.W., Partin, J., Jenson, J., Mylroie, J., Goddard, E., Quinn, T., Jocson, J. and Miklavič, B. (2012) Magnesium and strontium systematics in tropical speleothems from the Western Pacific. *Chemical Geology* **294-295**, 1-17.

68. Smith, A.J., Massuel, S. and Pollock, D.W. (2012) Geohydrology of the Tamala Limestone Formation in the Perth Region: Origin and role of secondary porosity. CSIRO, p. 63.

69. Spencer, C.N., Gabel, K.O. and Hauer, F.R. (2003) Wildfire effects on stream food webs and nutrient dynamics in Glacier National Park, USA. *Forest Ecology and Management* **178**, 141-153.

70. State Records Office of Western Australia (2015) Item CD1396 - Yonderup Cave, Yanchep, pp. Map of Yonderup Cave, Yanchep, Western Australia.

71. Stoof, C.R., Slingerland, E.C., Mol, W., van den Berg, J., Vermeulen, P.J., Ferreira, A.J.D., Ritsema, C.J., Parlange, J.-Y. and Steenhuis, T.S. (2014) Preferential flow as a potential mechanism for fire-induced increase in streamflow. *Water Resources Research* **50**, 1840-1845.

72. Treble, P., Shelley, J.M.G. and Chapell, J. (2003) Comparison of high resolution sub-annual records of trace elements in a modern (1911–1992) speleothem with instrumental climate data from southwest Australia. *Earth and Planetary Science Letters* **216**, 141-153.

73. Treble, P.C., Fairchild, I.J., Baker, A., Meredith, K.T., Andersen, M.S., Salmon, S.U., Bradley, C., Wynn, P.M., Hankin, S.I., Wood, A. and McGuire, E. (2016) Roles of forest bioproductivity, transpiration and fire in a nine-year record of cave dripwater

chemistry from southwest Australia. *Geochimica et Cosmochimica Acta* **184**, 132-150.

74. Valverde, J.M., Sanchez-Jimenez, P.E. and Pérez-Maqueda, L.A. (2015) Limestone calcination nearby equilibrium: kinetics, CaO crystal structure, sintering and reactivity. *The Journal of Physical Chemistry C* **119**, 1623-1641.
75. Wang, L., Xue, Z., Cai, J. and Hu, B. (2019) Relationship Between Microstructure and Properties of Limestone Calcined Rapidly at High Temperatures. *Transactions of the Indian Institute of Metals* **72**, 3215-3222.
76. Wang, J-J., Dahlgren, R.A., Erşan, M.S., Karanfil, T. and Chow, A.T. (2015) Wildfire altered terrestrial precursors of disinfection byproducts in forest detritus. *Environmental Science and Technology* **49**, 5921-5929.
77. Wang, Y., Cheng, H., Edwards, R.L., Kong, X., Shao, X., Chen, S., Wu, J., Jiang, X., Wang, X. and An, Z. (2008) Millennial- and orbital-scale changes in the East Asian monsoon over the past 224,000 years. *Nature* **451**, 1090-1093.
78. Weber, M., Scholz, D., Schröder-Ritzrau, A., Deininger, M., Spötl, C., Lugli, F., Mertz-Kraus, R., Jochum, K.P., Fohlmeister, J., Stumpf, C.F. and Riechelmann, D.F.C. (2018) Evidence of warm and humid interstadials in central Europe during early MIS 3 revealed by a multi-proxy speleothem record. *Quaternary Science Reviews* **200**, 276-286.
79. Wotton, B.M., Gould, J.S., McCaw, W.L., Cheney, N.P. and Taylor, S.W. (2012) Flame temperature and residence time of fires in dry eucalypt forest. International *Journal of Wildland Fire* **21**, 270-281.
80. Wu, G. and Wang, D.Y. (2012) Mechanical and acoustic emission characteristics of limestone after high temperature. *Advanced Materials Research* **446-449**, 23-28.